Mon. Not. R. Astron. Soc. **359,** 711–724 (2005) doi:10.1111/j.1365-2966.2005.08946.x

Doppler imaging and surface differential rotation of young open cluster stars – I. HD 307938 (R58) in IC 2602

S. C. Marsden,[1,2⋆] I. A. Waite,[1⋆] B. D. Carter[1⋆] and J.-F. Donati[3⋆]

[1]*Faculty of Sciences, University of Southern Queensland, Toowoomba, 4350, Australia*
[2]*Institut für Astronomie, ETH-Zentrum, CH-8092 Zürich, Switzerland*
[3]*Laboratoire d'Astrophysique, Observatoire Midi-Pyrénées, F-31400 Toulouse, France*

Accepted 2005 February 17. Received 2005 January 26; in original form 2004 August 31

ABSTRACT

In this paper we present Doppler images of a young active G dwarf (HD 307938) in the southern open cluster IC 2602. Spectroscopic data were obtained over a four-night period in 2000 January at the 3.9-m Anglo-Australian Telescope using the University College London Echelle Spectrograph. Simultaneous photometric observations (in the *V* and *R* bands) were obtained at the 1.0-m Australian National University telescope. By applying least-squares deconvolution (LSD) to the 2500+ photospheric lines in each echelle spectrum a single high signal-to-noise ratio LSD profile was produced for each phase of the spectroscopic observations. Maximum-entropy image reconstruction, incorporating both the LSD profiles and the photometric data, was used to produce maps of the surface features of the star, with the inclusion of the photometric data producing an increase (compared with the use of spectroscopic data alone) in the spot occupancy in both low- and mid-latitude regions of the star. The maps show that HD 307938 possesses a large, broken polar spot extending down to $\sim 60^\circ$ latitude, as well as lower-latitude spots similar to other rapidly rotating G dwarfs. By incorporating a solar-like differential rotation law into the imaging process the surface differential rotation of HD 307938 was determined. This gave a surface shear of $\mathrm{d}\Omega = 0.025 \pm 0.015$ rad d^{-1} (for an inclination angle of 60°). Thus the equator of HD 307938 laps the poles every $\sim$250 d and has a photospheric shear around half that of the Sun.

Key words: stars: activity – stars: imaging – stars: individual: HD 307938 – stars: late-type – stars: rotation.

1 INTRODUCTION

Magnetic activity on solar-type stars produces dark regions (star-spots) on the photospheres of these stars, as the eruption of the magnetic field through the stellar surface suppresses convection. With the advent of Doppler imaging it is now possible to map the distribution of these star-spots on rapidly rotating ($v \sin i \gtrsim$ 20 km s^{-1}) stars, offering an insight into the underlying magnetic dynamo. The requirement for rapid rotation means that Doppler imaging of solar-type stars is mainly limited to young stars on or near the zero-age main sequence (ZAMS), as the youthfulness of such stars is often associated with rapid rotation. A large sample of young, rapidly rotating solar-type stars can be found in young ($\lesssim$100 Myr) open clusters.

IC 2602 is a relatively young southern open cluster with an age of $\sim$30 Myr (Stauffer et al. 1997). This age means that the solar-type stars in IC 2602 should be on or arriving at the ZAMS and therefore the cluster contains a number of rapidly rotating solar-type stars suitable for Doppler imaging. Although IC 2602 is one of the closest known open clusters with a *Hipparcos* distance of $\sim$145 pc (van Leeuwen 1999), the solar-type F, G and K dwarfs in the cluster are still too faint for conventional single-line Doppler imaging. The faintness of the stars means that it is not possible to yield spectra with a high signal-to-noise (S/N) ratio (usually 200+), while at the same time keeping the exposure time low enough to reduce the effects of rotational blurring on spot features. The introduction of the method of least-squares deconvolution (LSD, Donati et al. 1997) has been used successfully to determine the surface structure on a number of stars too faint for single-line Doppler imaging (e.g. Barnes et al. 1998, 2000, 2001a,b, 2004a; Donati et al. 2000; Jeffers, Barnes & Collier Cameron 2002; Barnes, James & Collier Cameron 2004b). LSD utilizes the large number of photospheric lines available in an echelle spectrum to produce a least-squares profile that has a vastly increased S/N ratio over that of single-line data.

HD 307938 (also called R58 by Randich et al. 1995, the nomenclature which we will use in this paper) is a rapidly rotating

⋆E-mail: marsden@usq.edu.au (SCM); waite@usq.edu.au (IAW); carterb@usq.edu.au (BDC); donati@obs-mip.fr (J-FD)

($v \sin i = 93$ km s^{-1}, Stauffer et al. 1997; period = 0.57 d, Barnes et al. 1999) early-G dwarf in IC 2602 ($V \sim 10.6$, Stauffer et al. 1997) which shows photometric modulation attributable to non-axisymmetric star-spot coverage. This paper describes the Doppler imaging of R58 using the technique of LSD for data taken in 2000 January. Simultaneous multiband photometry has been used, along with the spectroscopic data, to help constrain the derived star-spot distribution. In addition, a solar-like differential rotation law has been incorporated into the Doppler imaging process to determine the surface differential rotation of R58.

2 OBSERVATIONS AND DATA REDUCTION

Simultaneous spectroscopic and photometric data were obtained for R58 over a four-night period in 2000 January (18th–21st inclusive). The spectroscopic data were obtained using the 3.9-m Anglo-Australian Telescope (AAT), while the photometric data were obtained using the 1.0-m Australian National University (ANU) telescope. Both of these telescopes are located at Siding Spring Observatory in New South Wales, Australia.

2.1 High-resolution AAT spectra

The spectroscopic data from the AAT were obtained using the University College London Echelle Spectrograph (UCLES). The detector used was the Deep Depletion MITLL3 charge-coupled device (CCD) with 2048 × 4096 15-μm^2 pixels. Since this chip is larger than the unvignetted field of the UCLES camera, a smaller window format (2048 × 2496 pixels) was used to reduce read-out time. Using the 31.6 groove mm^{-1} grating, 53 orders (order nos 77–129) could be fitted on to the reduced detector window, giving full wavelength coverage from 4375 to 7434 Å in a single exposure, with significant overlap (as much as half of the free spectral range for the bluest orders) between successive orders. The reduced detector window meant that vignetting within the UCLES camera for each order should only be ∼10 per cent larger on both order edges than at the order centre. With a slit width of 0.73 mm, or 1 arcsec (projecting on to 3.3 pixels at the detector level) a spectral resolution of around 48 000 (i.e. 6.3 km s^{-1}) was obtained, with an average pixel size of 1.9 km s^{-1}.

Using this setup, 21 usable 600-s exposures of R58 were collected on the night of 2000 January 18 under cloudy conditions. The next three nights were clear with ∼40 exposures collected on each of the last three nights, for a total of 139 usable exposures of the target. The seeing on all four nights was moderate to poor, from 1.3 arcsec up to 4.0 arcsec. A log of the AAT observations is given in Table 1.

2.1.1 Data reduction

All raw frames were converted into wavelength calibrated spectra using the ESPRIT (Echelle Spectra Reduction: an Interactive Tool) optimal extraction routines of Donati et al. (1997). A peak S/N ratio, in order no 89 (∼6385 Å), of 23–79 per 1.9 km s^{-1} pixel was obtained, depending upon the seeing and weather conditions during the exposure. For the spectra taken on 2000 January 18, order no 103 was removed from the reduced spectra as bad columns on the MITLL3 chip lay within the order. The spectrograph was shifted slightly for the remaining nights so that the bad columns were placed in the interorder gap.

Since the individual spectra of R58 have a low signal-to-noise ratio, normal single-line image reconstruction would be difficult as Doppler imaging requires the detection of signals with typical amplitudes of ∼1 per cent, requiring S/N ≫ 100. As the spectra for R58 were taken with an echelle spectrograph there are several thousand photospheric lines contained within each spectrum. Each of these lines are affected in a similar way by the presence of spot

Table 1. Log of spectroscopic AAT observations of R58 and template stars on 2000 January 18–21. The first two columns list the observation date and object name, while columns 3 and 4 give the start and end times of the sequence of exposures. Columns 5 and 6 give the exposure time for each observation and the number of usable exposures in the sequence. Column 7 gives the fractional rotational cycle (for R58 only) for the first and last exposure of each sequence, with zero phase taken as $04^h\ 05^m\ 50^s$ UT on the 20th. The template stars are: HD 8306 (G0 IV), HD 63077 (G0 V), moon (G2V), HD 64503 (B2 V) and HD 85512 (M0 V).

UT date	Object	UT start	UT end	Exposure time (s)	No. of frames	Rotational cycle
2000 Jan 18	HD 8306	10:12	10:22	600	1	
	HD 63077	10:25	10:30	300	1	
	HD 64503	10:33	10:38	300	1	
	HD 85512	10:40	10:50	600	1	
	Moon	10:53	10:54	60	1	
	R58	10:58	16:55	600	21	−3.000 to −2.577
2000 Jan 19	HD 8306	10:17	10:27	600	1	
	HD 64503	10:30	10:35	300	1	
	HD 63077	10:37	10:42	300	1	
	HD 85512	10:44	10:54	600	1	
	R58	11:01	18:48	600	39	−1.242 to −0.700
2000 Jan 20	HD 8306	10:01	10:11	600	1	
	HD 64503	10:15	10:20	300	1	
	HD 63077	10:22	10:27	300	1	
	HD 85512	10:29	10:39	600	1	
	R58	10:41	18:46	600	39	0.488 to 1.038
2000 Jan 21	HD 8306	09:47	09:57	600	1	
	HD 64503	10:01	10:06	300	1	
	HD 63077	10:08	10:13	300	1	
	HD 85512	10:16	10:26	600	1	
	R58	10:29	18:51	600	40	2.227 to 2.799

features in the stellar photosphere. LSD (Donati et al. 1997) allows the extraction of the intensity information from as many of these lines as possible and combines them into a single high S/N ratio profile. To produce the LSD profiles of R58 we used spectral features with a relative central depth larger than 0.4 (over 2500 in all) taken from a G2 line list created from the Kurucz atomic data base and ATLAS9 atmospheric models (Kurucz 1993). Very strong lines, such as the Balmer lines have been not been included as well as lines near high densities of tellurics such as around 6875 Å. The LSD profiles produced had S/N ratio values from 318 to 1044 per 2 km s^{-1} bin. This corresponds to an average multiplex gain of ∼13–14 over that of single-line data. The S/N ratio values of the LSD profiles are calculated from the errors propagated through the deconvolution process. This has the effect of underestimating the S/N ratio of the LSD profiles and thus the multiplex gain may be slightly higher than stated here. This underestimation of the S/N ratio also has the effect that the images in Section 4 are reconstructed with reduced χ^2 values less than 1.0, similar to that of Petit et al. (2004). This has no effect on the results presented. Further information on LSD can be found in Wade et al. (2000) and Donati et al. (1997).

In order to remove any shifts in the spectrograph during the night, each wavelength-calibrated spectrum was shifted to match the LSD profile of the telluric lines contained in the spectrum. This should reduce the relative radial velocity shifts of the LSD profiles to less than 0.1 km s^{-1}.

2.2 Photometry

The photometric observations of R58 were taken in both V and R bands (standard Johnson–Cousins system) using an EEV 2k × 1k CCD (MSSSO, CCD6) with 22-μm^2 pixels, mounted at the coudé focus of the 1.0-m ANU telescope. Fig. 1 shows a trimmed CCD image of the target field, with the target (R58) and comparison stars indicated.

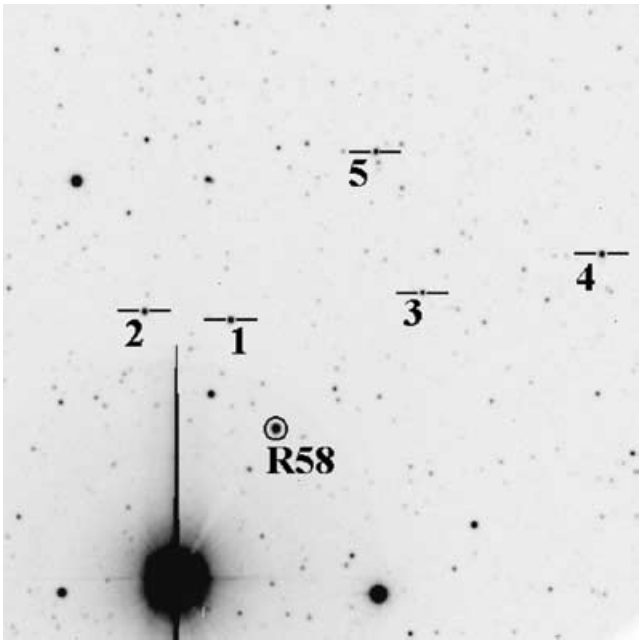

Figure 1. Finder chart showing the location of the target star, R58 and five comparison stars with north and east located up and left, respectively. The brightest star in the image is Θ Carinae. The field size is approximately 11 × 11 $arcmin^2$.

2.2.1 Data reduction

The images were reduced using IRAF. The CCD frames were originally trimmed to remove both the overscan region and the defective columns that were present on one side of the CCD image. Each night a number of calibration frames were taken, including bias frames, dark current frames and flats. The calibration frames were combined to produce nightly master frames in each case. The stars in the frame were found using DAOFIND and synthetic aperture photometry was performed using DAOPHOT. The sky background was calculated and removed using the mode of an annulus around the synthetic aperture.

Along with observations of the target (R58), observations of the standard stars in Graham's E4 region (Graham 1982) were also taken during the run. Using four of the standard stars in the E4 region (stars a, d, h and K, the others being either too faint to be useful or lying off the CCD) the following transformation equations were solved:

$$V = v - v_0 - v_1 X_v - v_2(V - R) \quad (1)$$

$$R = r - r_0 - r_1 X_r - r_2(V - R), \quad (2)$$

where V and R are the listed magnitudes of the standard stars in Graham (1982) in the V and R bands, v and r are the observed instrumental magnitudes of the standard stars, X_v and X_r are the airmass of the observations, v_0 and r_0 are the zero-points for zero airmass, v_1 and r_1 are the extinction coefficients, and v_2 and r_2 are the colour correction coefficients. The values determined for the coefficients are given in Table 2.

It should be noted that we have used the V and R magnitudes for the four standard stars as listed in Graham (1982). However, Sung & Bessell (2000), in a CCD study of Graham's E-regions, found that for the fainter stars ($V > 12$) the magnitudes they measured were systematically fainter by 0.05 mag compared with those measured by Graham (1982). We have chosen to use the original Graham values as the Sung & Bessell study did not specifically observe the E4 region used here.

Using equations (1) and (2), the magnitudes of the five comparison stars in Fig. 1 were determined. This was performed iteratively until the change in $(V - R)$ was less than 0.001 mag. The colours for the five comparison stars in Fig. 1 are listed in Table 3.

As Table 3 shows, the magnitudes of the five comparison stars are significantly less than that of our target R58 ($V \sim 10.6$). The

Table 2. Transformation coefficients for equations (1) and (2) for 2000 January CCD photometry.

x	v_x	r_x
0	−2.347	−2.724
1	0.108	0.057
2	−0.220	−0.042

Table 3. Colours of the five comparison stars used in the analysis of 2000 January CCD photometry. The star numbers correspond to those listed in Fig. 1.

Star number	V	R	$(V - R)$
1	12.223	11.527	0.696
2	12.389	11.868	0.521
3	12.948	12.671	0.277
4	12.344	11.587	0.757
5	12.594	11.901	0.693

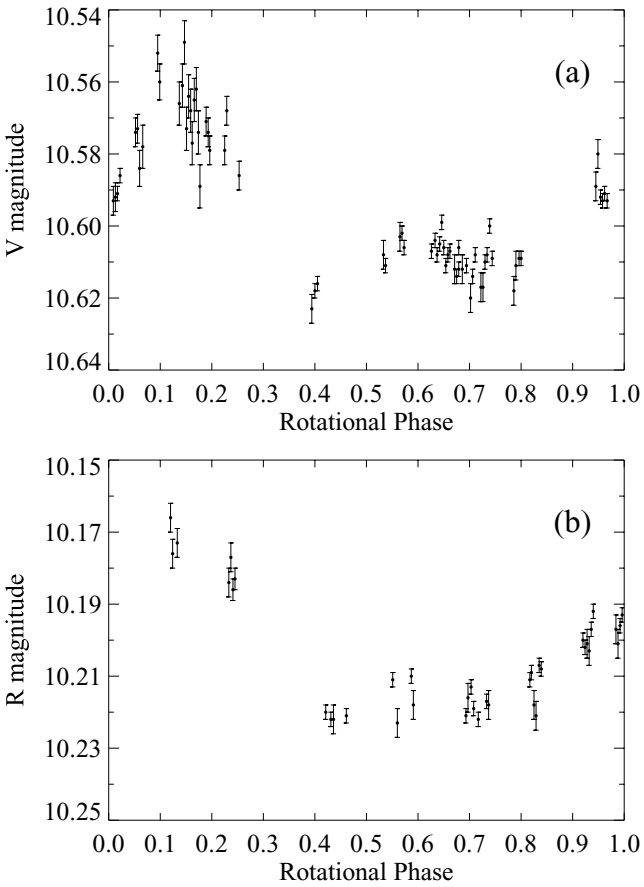

Figure 2. Light curves in (a) V and (b) R for R58, 2000 January 19–21. The magnitudes are above-atmosphere values. The error bars represent the error in individual measurements as calculated by DAOPHOT.

other brighter stars in Fig. 1 often saturated or showed evidence of variability making them unsuitable. As a result of the faintness of the comparison stars, the counts from all five stars listed in Table 3 were combined (with colour correction terms) to produce differential photometry of R58. This differential photometry was then converted to above-atmosphere magnitudes using equations (1) and (2). As a check the five comparison stars were compared with each other for variability.

The above-atmosphere light curves (in both V and R) for R58 are shown in Fig. 2 for the nights of 2000 January 19–21. Severe winds on the night of January 18 meant that no photometric data were obtained for that night. The light curves in Fig. 2 are plotted against the rotational phase of R58. This was calculated based on a period for R58 of 0.57 d, measured by Barnes et al. (1999), as our photometry was too limited to acquire an accurate measurement of the rotational period. These observations give a $(V - R_C)$ for R58 of $\sim$0.39, very similar to the value of 0.40 found by Prosser, Randich & Stauffer (1996).

3 IMAGE RECONSTRUCTION

The surface images of R58 were obtained using both the spectroscopic LSD line profiles (obtained on all four nights, 2000 January 18–21 inclusive) and photometric (V- and R-band) light curves (obtained on the last three nights, 2000 January 19–21 inclusive). As mentioned previously no photometric data for R58 were obtained on the 18th. The R-band magnitudes shown in Fig. 2(b), were brightened by 0.02 to account for the reddening of IC 2602. Whiteoak (1961) gives a value for the reddening of the cluster IC 2602 as $E(B - V) = 0.04$. Using this value, we determined $E(V - R_C) = 0.02$ based on

$$\frac{E(V-R)}{E(B-V)} = 0.58 + 0.09(V-R) \quad (3)$$

taken from Bessell, Castelli & Plez (1998).

A rotational period of 0.57 d meant that complete phase coverage of the star could be obtained in three nights of observations, with over two-thirds of the phase of the star being observed at least twice. Table 1 shows that the spectroscopic observations of R58 span almost six rotations of the star.

The imaging code used to perform brightness imaging on the stellar surface of R58 is the code of Brown et al. (1991) and Donati & Brown (1997), which implements the Skilling & Bryan (1984) algorithm for maximum-entropy optimization. This technique produces images with the minimum amount of information (surface features) required to produce the observed photometric and spectroscopic intensity variations. The code uses a two-component brightness model (one for spots and one for the quiet photosphere, as described by Collier Cameron 1992), where for each image pixel the local relative area occupied by cool spots is reconstructed. This is called spot occupancy.

By determining the best fit to the spectroscopic and photometric data (see Section 4) the photospheric and spot temperatures for R58 were found to be 5800 and 3900 K, respectively. These temperatures correspond to roughly a G2 and an M0 star, respectively. The G2V standard star observed was the Sun (via reflected moonlight) while the M0V standard observed was HD 85512 (see Table 1). These are the same stars as used by Donati et al. (2000) in the Doppler imaging of the G dwarf LQ Lup (RX J1508.6-4423). The LSD profiles of the moon and HD 85512, both created using a G2 line mask (the same line mask used to create the R58 LSD profiles), are shown in Fig. 3. Instead of using the LSD profiles of these standard stars as representations of the photosphere and spots of R58, as was performed by Donati et al. (2000) for LQ Lup, we have used synthetic Gaussian profiles of similar full-width half-maximum (FWHM) as the standard stars. Gaussian profiles have previously been used in Doppler imaging by Petit, Donati & Collier Cameron (2002) and Petit et al. (2004). Gaussian profiles were chosen over the standard star profiles as the Doppler imaging code tends to converge more smoothly. The Gaussian chosen to represent both the spot and

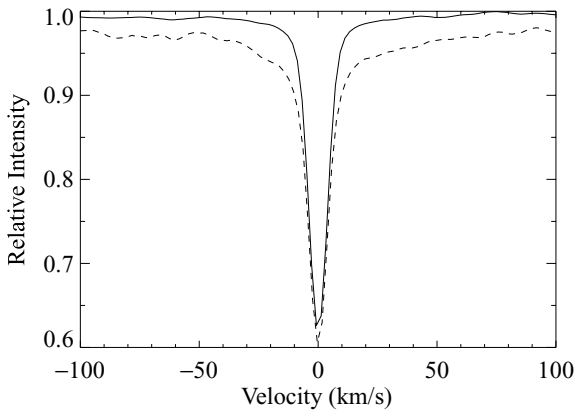

Figure 3. LSD profiles for the moon (solid line) and HD 85512 (dashed line). Both profiles were created using a G2 line mask and have been recentred to zero radial velocity.

the photospheric profiles had a FWHM of 10 km s^{-1} matching the LSD profile of the moon in Fig. 3. Unlike Petit et al. (2004) we have used the same Gaussian for both the spot and the photosphere as the central depth of both LSD profiles in Fig. 3 is similar. The results of Unruh & Collier Cameron (1995) show that Doppler images reconstructed from a Gaussian profile are almost identical to those obtained using a standard star.

The Doppler imaging code is capable of incorporating both spectroscopic and photometric observations into the image reconstruction process. The emphasis placed on the photometric data is determined by the weighting assigned to it. For the R58 images in Section 4 a weighting of 1.0 was assigned to the photometric data. A weighting of 1 on both data sets means that the relative weighting for each spectroscopic and photometric data point is equal to $1/\sigma_i^2$, where σ_i is the error bar associated with point i.

4 THE SURFACE FEATURES OF R58

To determine the parameters used in the maximum-entropy reconstruction, a χ^2 minimization technique was employed (see Barnes et al. 2000). In this method the parameters that simply give the best fit to the data (lowest reduced χ^2 values) are chosen. Using this method the parameters for R58 listed in Table 4 were found.

The maximum-entropy image reconstruction of the spot distribution of R58, using the values in Table 4, is shown in Fig. 4. Fits to the spectroscopic data for the four nights are given in Fig. 5. The spot filling factor given in the caption of Fig. 4 (and others) gives the fraction of the entire stellar surface occupied by spots. This is an underestimation of the amount of spot coverage on the star for two reasons. First, only one hemisphere of the star can realistically be mapped (some features in the southern hemisphere can be determined, but due to limb darkening these features are very faint and thus little of the southern hemisphere is reconstructed) and secondly, the maximum-entropy method used in the Doppler imaging process inherently gives the minimal number of spots required to produce the observed line profiles. This last point is of less importance when high S/N ratio data are used.

Using the values in Table 4 and the isochrones of Siess, Dufour & Forestini (2000) along with the *Hipparcos* distance to the cluster of $(m - M)_V = 5.81 \pm 0.06$ (van Leeuwen 1999), corresponding to a distance of 145 ± 4 pc, implies that R58 is a $\sim$1.15 solar-mass star with an age of $\sim$35 Myr.

Table 4. Listing of parameters found for R58 in the maximum-entropy image reconstruction of the star. The stellar mass and age are based on isochrones from Siess et al. (2000) and the inclination angle and stellar radius were estimated as described in Section 4.2. The equatorial rotation period has been calculated for an inclination angle of 60°, see Section 4.3.

Parameter	Value
$v \sin i$	92 ± 0.5 km s^{-1}
Radial velocity ($v_{\rm rad}$)	12.7 ± 0.1 km s^{-1}
Inclination angle (i)	$60^\circ \pm 10^\circ$
Photospheric temperature ($T_{\rm P}$)	5800 ± 100 K
Spot temperature ($T_{\rm S}$)	3900 ± 100 K
Photosphere–spot difference	1900 ± 200 K
Equatorial rotational velocity ($v_{\rm eq}$)	106^{+15}_{-9} km s^{-1}
Equatorial rotational period ($P_{\rm eq}$)	0.5641 ± 0.0004 d
Unspotted V magnitude	10.36 ± 0.02 mag
Stellar radius (R)	$1.18^{+0.17}_{-0.10}\,{\rm R}_\odot$
Stellar mass (M)	$1.15 \pm 0.05\,{\rm M}_\odot$
Age	35 ± 5 Myr

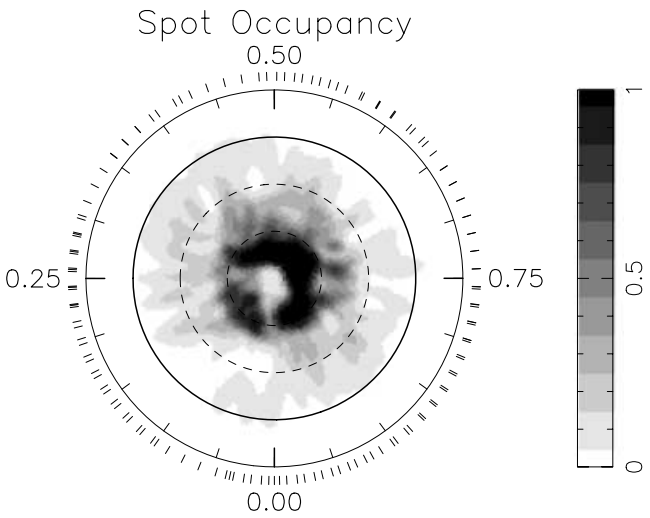

Figure 4. Maximum-entropy brightness image reconstruction for R58, 2000 January 18–21. The image is a flattened polar projection extending down to a latitude of −30°. The bold line denotes the equator and the dashed lines are +30° and +60° latitude parallels. The radial ticks outside the plot indicate the phases at which the star was observed spectroscopically. Note the polar spot appears as a polar ring (presumably due to solar contamination in the centre of the line profile, see Section 4.1 for details). This image has a spot filling factor of 0.13 (or 13 per cent).

4.1 Removing solar contamination

As can be seen in Fig. 5, there is a dip in the middle of most of the observed LSD profiles. This dip is due to reflected moonlight being scattered into the spectrograph and is most notable on the night of the 18th when there was a great deal of cloud present. Although the last three nights of the run appeared to be clear, some moonlight still appears to have been scattered into the spectrograph on these nights. As these observations were taken around the time of full moon, the moon was up for almost the entire run, except for the 18th when the moon set towards the end of the observations of the night. As can be seen in Fig. 5(a) the last three profiles on the 18th show little or no evidence of a central dip, supporting the idea that the contamination in the other profiles is due to reflected moonlight. The magnitude of the terrestrial velocity towards R58 during the observing run was very similar to the radial velocity of R58, meaning that the dip appears in the centre of the LSD profile. This makes it difficult to recover the spot distribution at the very pole of the star.

As an initial attempt to make sure that the contamination in the observed LSD profiles did not strongly affect the model fit to the data, the Doppler imaging code was modified so that the error bars in the central part of the profiles (−5.0 to +9.0 km s^{-1}, the region of contamination) were inflated to $\sqrt{100}$ times the normal size (any large number would suffice). This was performed for all profiles except for 17 profiles on the 19th (the profiles with underlined phases in Fig. 5b). These 17 profiles had their error bars kept as normal, as they appear to show little or no contamination. Where inflated error bars were used, it meant that the Doppler imaging code would be less likely to try and fit the contaminated data in these central regions. However, the resultant image in Fig. 4 shows that some fitting of the contamination still occurs as the image has little features at the very pole.

In order to remove the contamination due to scattered moonlight from the observed LSD profiles, the modelled LSD profiles created in the initial pass through the Doppler imaging code were subtracted

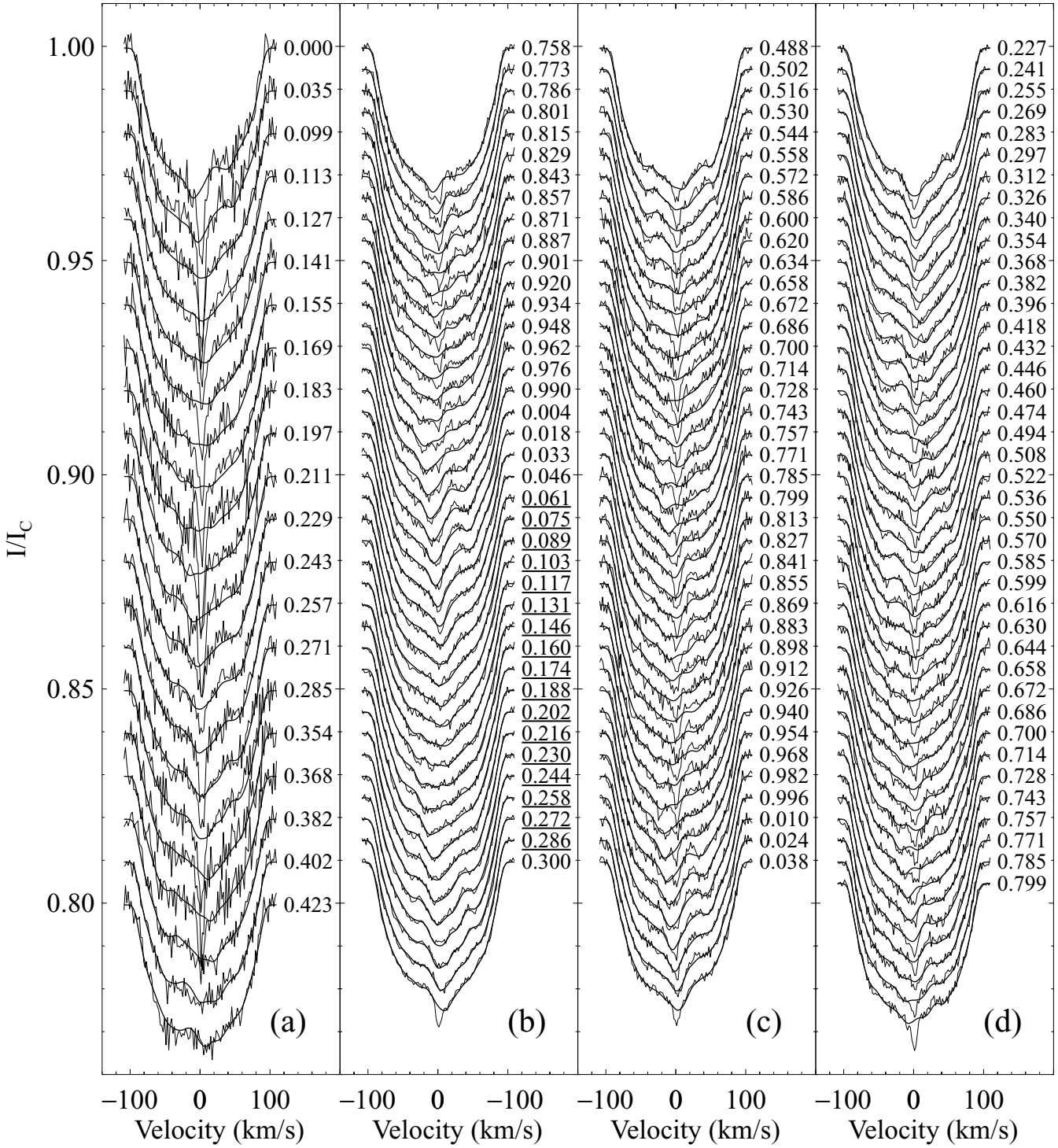

Figure 5. Maximum-entropy fits to the LSD profiles for R58, for 2000 January (a) 18, (b) 19, (c) 20 and (d) 21. The thin lines represent the observed LSD profiles while the thick lines represent the fits to the profiles produced by the Doppler imaging code. For the 18th each successive profile is shifted down by 0.01 for graphical purposes and the shift is 0.005 for the other nights. The rotational phases at which the observations took place are indicated to the right of each profile. The underlined phases represent those profiles apparently relatively free of contamination as described in Section 4.1.

from the observed LSD profiles and a scaled LSD profile of the moon (taken with the same instrumental setup) was fitted to these difference profiles. This scaled moon profile was then subtracted from the observed LSD profiles, removing the contamination. The amount of scaling required is different for each profile, as it is dependent upon the level of contamination in each profile. This level of contamination was determined by minimizing the following equation for each difference profile:

$$\sum_{i=-v\sin i}^{+v\sin i} (y_i - \alpha z_i)^2, \tag{4}$$

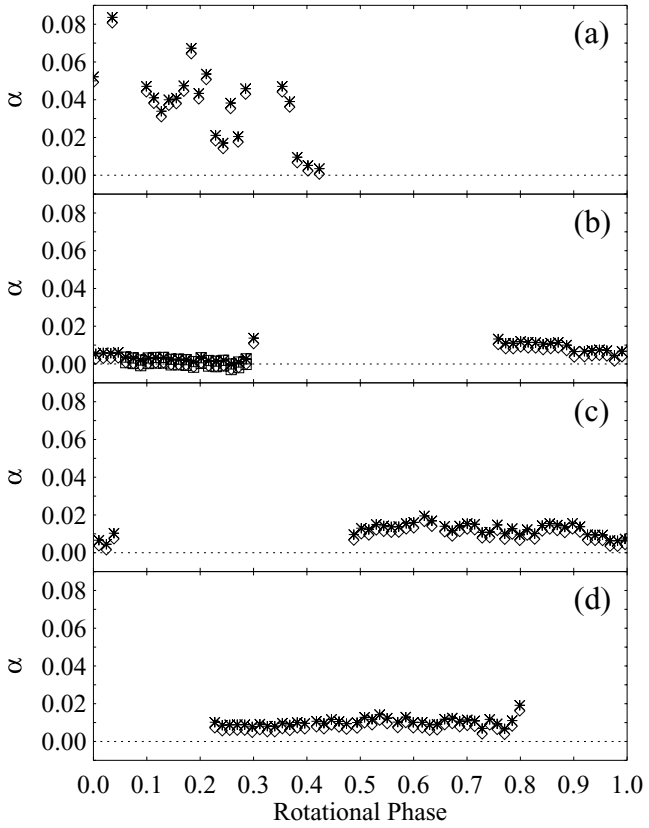

Figure 6. Degree of spectral contamination (α) in the observed LSD profiles for 2000 January (a) 18, (b) 19, (c) 20 and (d) 21. Diamonds represent the initial measured α values and stars the α values used in the removal of the spectral contamination, see Section 4.1 for details. The boxed data points, on the 19th, show the alpha values for those profiles apparently relatively free of contamination, again see Section 4.1.

where y is the difference profile, z is the inverted moon profile and α is the contamination level. The level of contamination determined by this method for each profile is shown as diamonds in Fig. 6.

This technique is not perfect as some of the contamination may be fitted in the modelled LSD profiles. This could lead to an underestimation of the amount of solar contamination and usually results in no polar features in the resultant image, as the default spot occupancy is defined as zero. Using the level of contamination determined from the above method did in fact result in an image still showing little features at the pole.

The 17 LSD profiles on the 19th, chosen for their low contamination, show contamination levels around zero or, for many of these profiles, a negative contamination level, seen as a negative α value in the boxed data points in Fig. 6(b). Assuming that this negative value is the result of the model fitting some of the contamination and thus underestimating it, we have set the most negative value of α (assumed to be the least contaminated profile) equal to zero and shifted up all other values of α by this amount in an attempt to obtain a more realistic representation of the amount of contamination in the profiles. The α values used in the removal of the solar contamination are shown in Fig. 6 as stars. Running the Doppler imaging code again with no inflated error bars and the contamination removed from the LSD profiles, produced the image shown in Fig. 7. The fits to the contamination-subtracted LSD profiles are shown in Fig. 8 and the fits to the photometric data (along with the residuals for the photometric data) are given in Fig. 9.

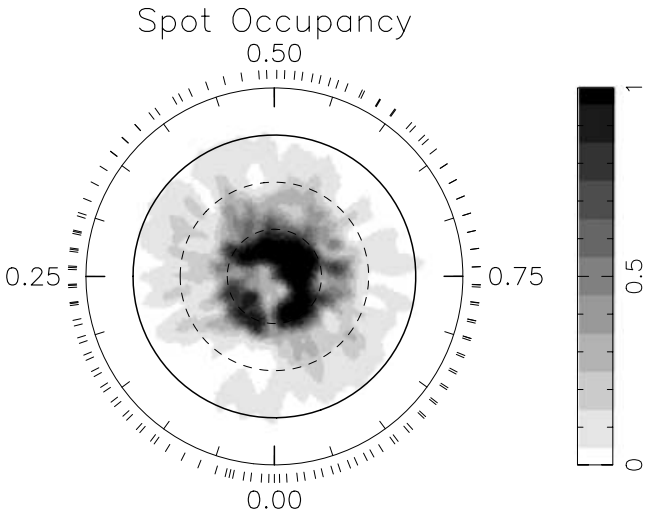

Figure 7. Maximum-entropy brightness image reconstruction for R58, 2000 January 18–21, with the contamination removed from the LSD profiles. The image is a flattened polar projection as described in Fig. 4 and has a spot filling factor of 0.13.

Dynamic spectra of the observed and modelled LSD profiles are shown in Figs 10–13. The observed LSD profiles have had the mean observed LSD profile subtracted from them, while the modelled LSD profiles have had the mean modelled LSD profile subtracted from them, in order to highlight the spot signatures. The residuals of the LSD profiles are created by subtracting the modelled LSD profiles from the observed ones. A comparison of the observed and modelled LSD profiles shows that features present in the observed profiles are found in the modelled profiles. The observed LSD profiles for the 18th (Fig. 10) are of poor quality and the modelled features are mainly derived from overlapping phase data on the other three nights. If the Doppler imaging code is either modelling features that do not exist or fails to model features present in the LSD profiles, this would be evident in the fits to the spectroscopic data. Features that the modelled data did not include would appear as dark bands passing from the blue wing to the red wing of the profile and as diagonal bands in the residual images. Features that the modelled data incorporated that were not in the original data would appear as white bands passing from the blue to the red wing. Looking at the residuals in Figs 10–13, there would appear to be no such features present. The scale of the residual dynamic spectra plots is $\pm 2.5 \times 10^{-3}$ which is ± 0.25 per cent of the continuum intensity of the profile.

Figs 4 and 7 show the reconstructed image using both the spectroscopic and photometric data with a weighting of 1.0 placed on both. In order to determine the usefulness of photometric data in the reconstruction of surface features, Fig. 14 shows the image reconstruction using only the spectroscopic data.

The variation in spot occupancy with stellar latitude for the images created using spectroscopy alone and spectroscopy plus photometry (along with variations in the inclination angle, Section 4.2) is given in Fig. 15, which plots fractional spottedness versus stellar latitude. Fractional spottedness is defined as

$$F(l) = \frac{S(l)\cos(l)\,\mathrm{d}l}{2}, \tag{5}$$

where $F(l)$ is the fractional spottedness at latitude l and $S(l)$ is the average spot occupancy at latitude l.

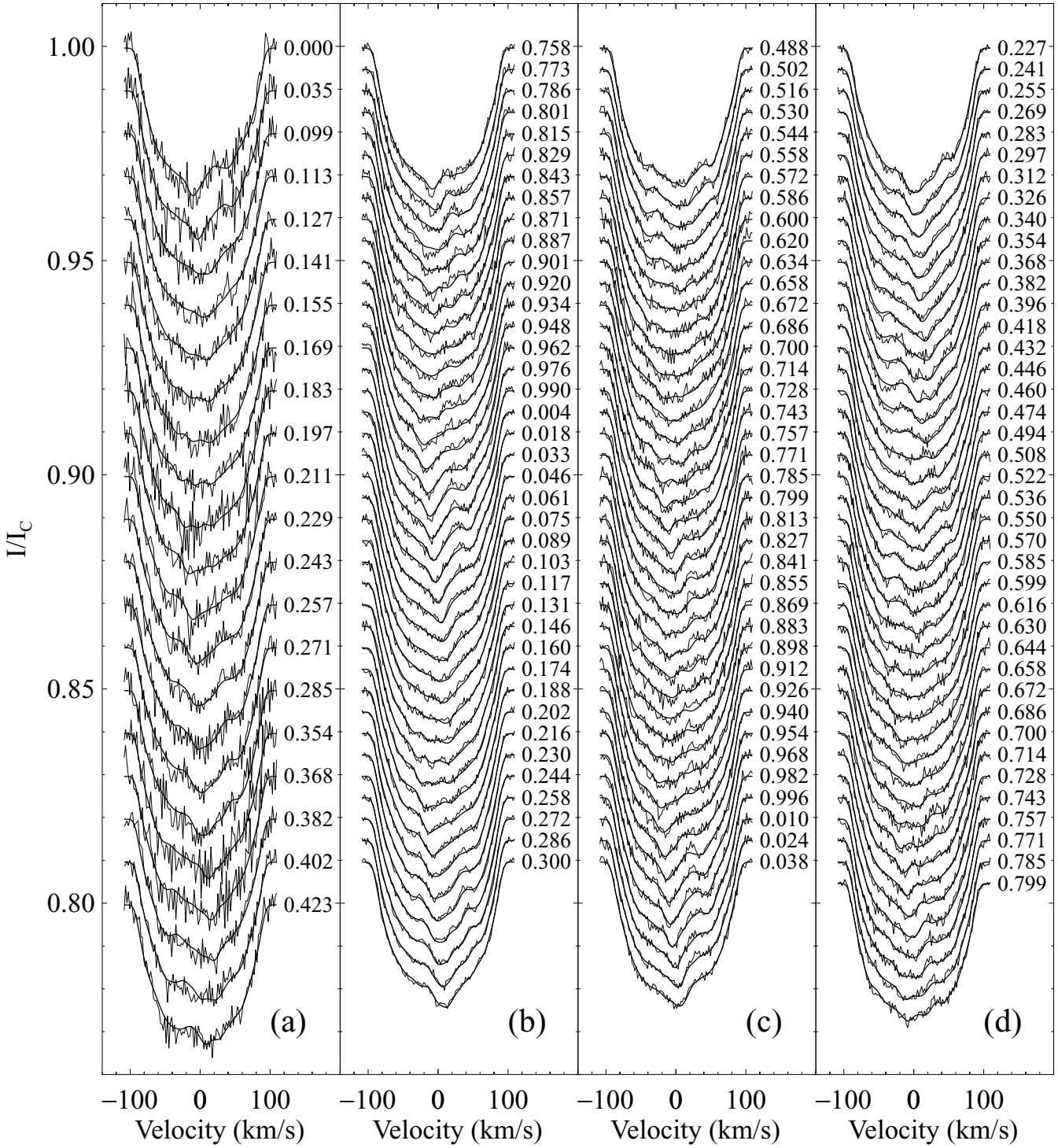

Figure 8. Maximum-entropy fits to the LSD profiles for R58, for 2000 January (a) 18, (b) 19, (c) 20 and (d) 21, with the contamination removed from the LSD profiles. The figure is as described for Fig. 5.

While the overall structure of the surface features is retained when comparing Fig. 7 (incorporating photometry) and Fig. 14 (without photometry), the inclusion of photometry in the image reconstruction has the result of enhancing the lower-latitude features of the star. The total spot coverage of the star incorporating photometry is ∼13 per cent while the coverage is ∼9 per cent when no photometry is included. Fig. 15 shows that not only are the low (−30° to +30°) latitude features enhanced with the inclusion of photometry, but that there is a significant increase in the spot occupancy for the mid-latitude (+30° to +60°) features as well. The high-latitude (+60° to +90°) regions are less affected by the inclusion of photometry.

In order to determine if the resultant images in Figs 4, 7 and 14 are fitting noise rather than data, independent reconstructions from the odd- and even-numbered LSD profiles were carried out and are plotted in Fig. 16. These odd and even images appear to show the same structure as each other and that of the overall map (Fig. 7).

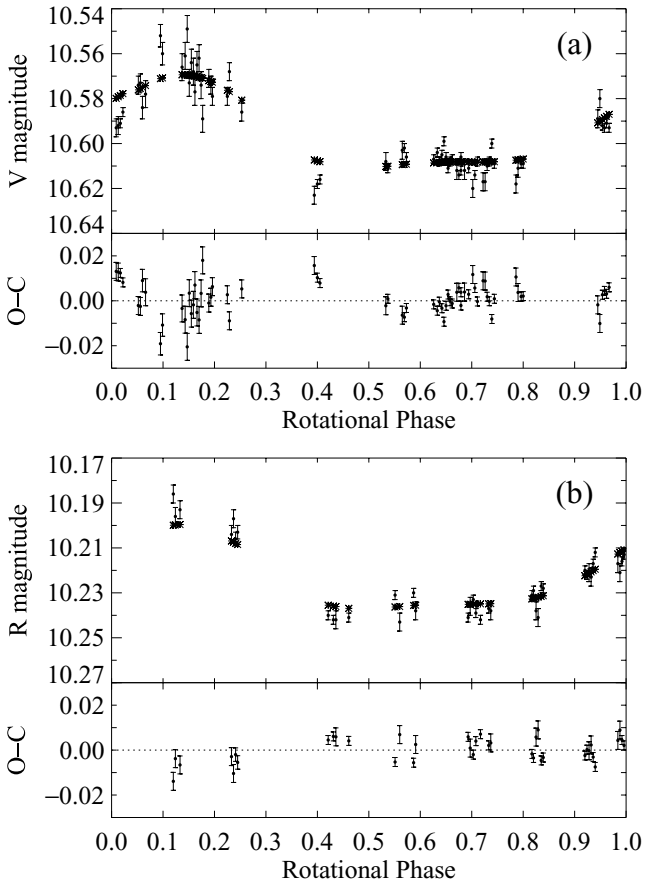

Figure 9. Photometric light curves (points with error bars) in (a) *V* and (b) *R* and maximum-entropy fits (stars) for R58, 2000 January 19–21. The top graph in each image plots the light curves and the maximum-entropy fits. The bottom graph in each image plots the fit to the light curve (observed–calculated). The magnitudes are above-atmosphere values.

This indicates that the image produced is an accurate (though spot-content minimized) representation of the surface structure of R58.

4.2 Determining inclination angle

The most difficult parameter to constrain with Doppler imaging is the axial inclination of the star. Using the χ^2 minimization method gives an inclination angle for R58 of $\sim 50^\circ$, see Fig. 17.

Alternatively, the axial inclination can be estimated from the bolometric magnitude of the star, giving its radius (see Bessell et al. 1998). Using the unspotted *V* magnitude of R58 from Table 4, the *Hipparcos* distance modulus to IC 2602 and a bolometric correction of -0.06 (corresponding to an effective temperature of 5800 K from Bessell et al. 1998) the absolute bolometric magnitude of the (unspotted) star is 4.55. This implies that R58 has a radius of $1.08\,R_\odot$. Given a $v \sin i = 92$ km s^{-1} and a rotational period of 0.5641 d (both from Table 4), the inclination angle of R58 is calculated to be $\sim 70^\circ$. This is significantly higher than the value of 50° obtained using the χ^2 minimization method and Fig. 17 shows that the reduced χ^2 fit for an inclination angle of 70° is significantly above that for 50°.

A value of 60° for the inclination angle was chosen to create the Doppler images of R58. This value importantly has a reduced χ^2 fit (Fig. 17) not significantly increased from that of 50°.

The isochrones of Siess et al. (2000) give an estimated radius of 1.00–1.13 $R_\odot$ for a 30–40 Myr old, 1.1–1.2 $M_\odot$ star. Using a value of $i = 60^\circ$ gives a radius for R58 of $1.18\,R_\odot$, as given in Table 4. Although this is larger than those given by Siess et al., the high rotation rate of R58 could lead to a larger equatorial radius due to possible oblateness of the star. Inclination angles of 50° and 70° give radii of 1.34 and $1.09\,R_\odot$, respectively. The radius for an inclination angle of 50° is significantly higher than the above-mentioned Siess et al. (2000) model values.

As a comparison, the images of R58 produced using axial inclinations of 50° and 70° are shown in Fig. 18. The variation in fractional

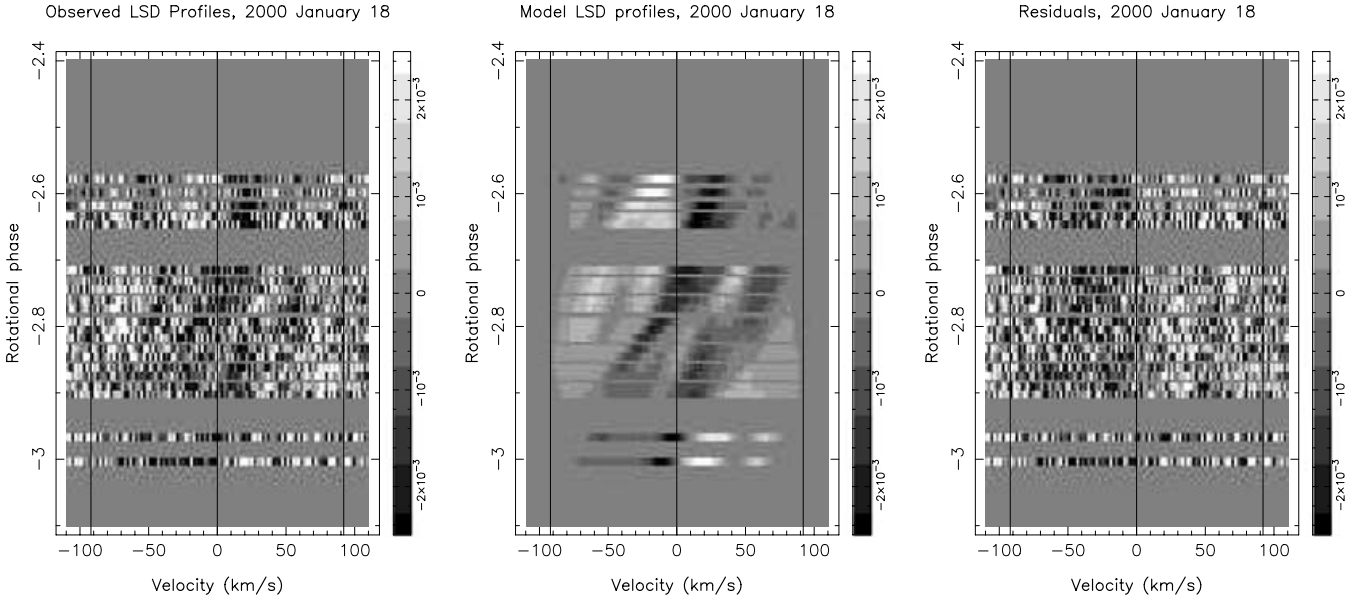

Figure 10. Dynamic spectra of the LSD profiles for R58 on 2000 January 18. The observed and modelled profiles have had the mean observed and modelled LSD profile, respectively, subtracted to enhance the spot features. The residual profiles have been created by subtracting the modelled LSD profiles from the observed ones. All profiles are centred on the radial velocity of R58. The three vertical lines on the images show the centre of the line profile (middle line) and the rotational broadening of the line profile (outer lines). Zero phase has been taken as $04^h\,05^m\,50^s$ UT on 2000 January 20.

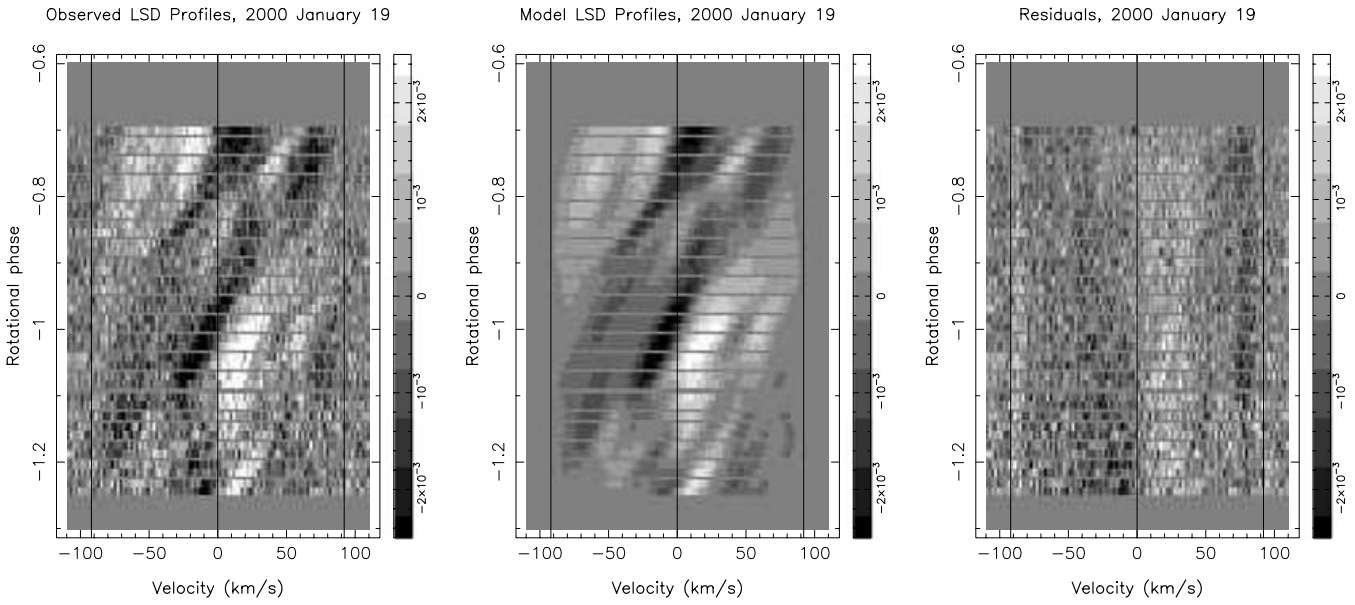

Figure 11. Same as in Fig. 10 for 2000 January 19.

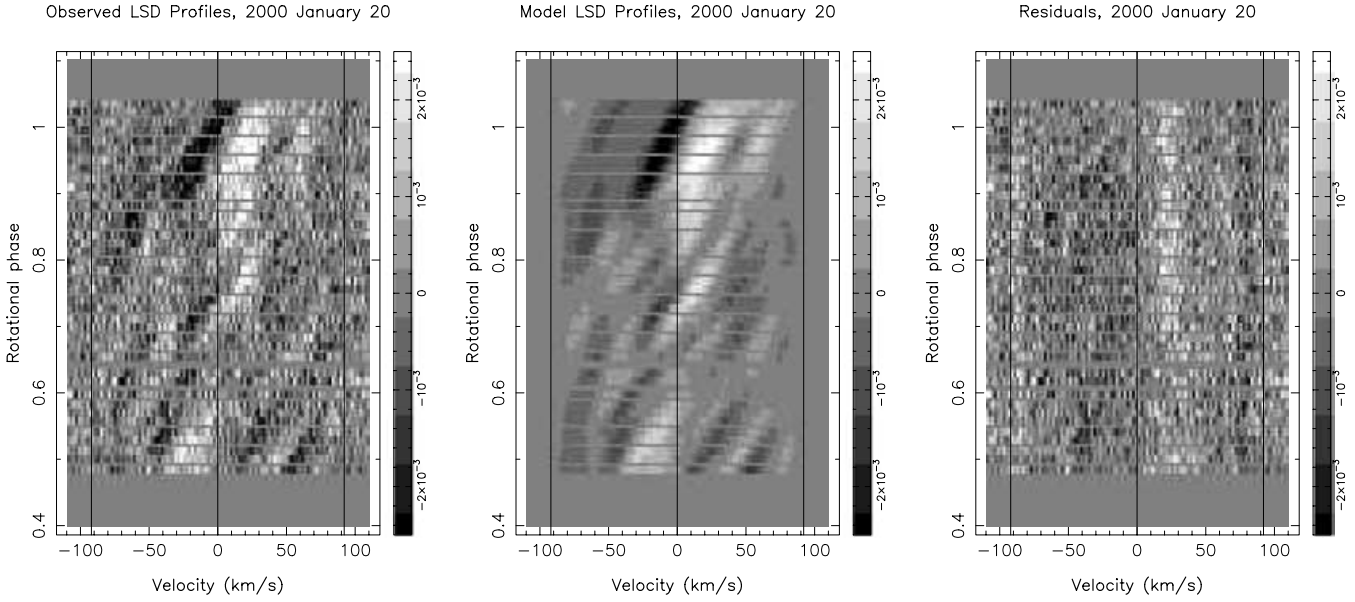

Figure 12. Same as in Fig. 10 for 2000 January 20.

spottedness (equation 5) with stellar latitude for the differing inclination angles is given in Fig. 15.

A comparison of the images in Figs 7 and 18 shows that the images retain the same overall structure, but with less spot filling for an inclination of 50° and more for an inclination of 70°. The spot coverage of the total stellar surface is ∼10 per cent using an inclination angle of 50°, ∼13 per cent using an inclination angle of 60° and ∼17 per cent using an inclination angle of 70°. Fig. 15 shows that while the amount of spot coverage is increased at all latitudes with an increase in the inclination angle, it is primarily the mid- and high-latitude regions that are affected by the change in the modelled inclination angle of the star.

4.3 Surface differential rotation

The surface differential rotation of a star can be measured from the rotation of spot features at different latitudes on the stellar surface. In an attempt to measure the surface differential rotation on R58, a solar-like differential rotation law was assumed, as has been found in stars that have previously had differential rotation measured (see Barnes et al. 2005):

$$\Omega(l) = \Omega_{\rm eq} - {\rm d}\Omega \sin^2 l \ ({\rm rad\ d}^{-1}), \qquad (6)$$

where $\Omega(l)$ is the rotation rate at latitude l, $\Omega_{\rm eq}$ is the equatorial rotation rate and dΩ is the rotational shear between the equator and

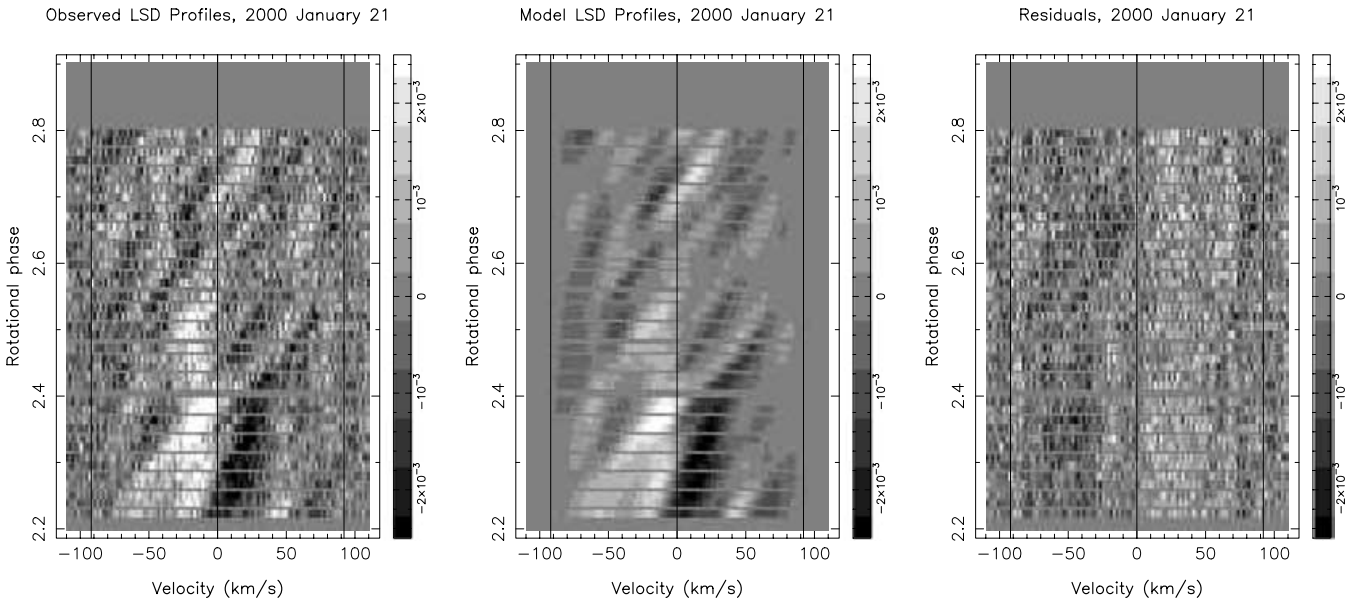

Figure 13. Same as in Fig. 10 for 2000 January 21.

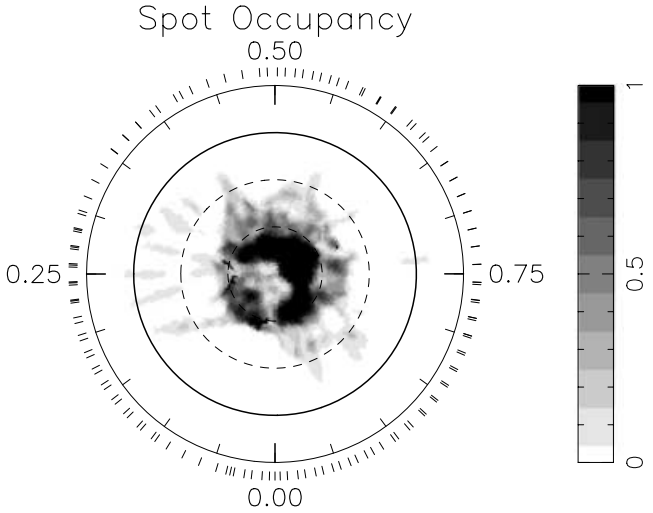

Figure 14. Maximum-entropy brightness image reconstruction for R58, 2000 January 18–21, using spectroscopic data alone (with contamination removed). The image is a flattened polar projection as described in Fig. 4, and has a spot filling factor of 0.09.

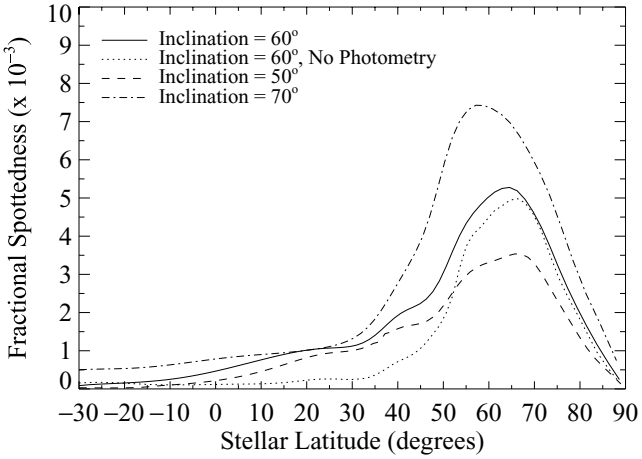

Figure 15. Fractional spottedness versus stellar latitude for various images of R58. Fractional spottedness is based on the average spot occupancy at each latitude and is defined by equation (5).

the pole. The differential rotation can be measured by incorporating equation (6) into the imaging process. By considering both Ω_{eq} and dΩ to be free parameters, the best fit to the data set can then be determined by a χ^2 minimization method, as outlined by Petit et al. (2002).

This method was used on the R58 data to determine the differential rotation by fitting to the spectroscopic data alone and forcing the Doppler imaging code to converge to a fixed spot filling factor of 0.09 in this case (the level of spot coverage produced by the map when photometry is not included, Fig. 14), for various values of Ω_{eq} and dΩ. The differential rotation is then determined by fitting a paraboloid to the reduced χ^2 values. The reduced χ^2 levels for various values of Ω_{eq} and dΩ for R58, with a modelled inclination angle of 60°, are shown in Fig. 19.

Fitting the derived paraboloid in Fig. 19 yields values for Ω_{eq} and dΩ of 11.139 and 0.025 rad d^{-1}, respectively, with 1σ errors for Ω_{eq} and dΩ of 0.008 and 0.015 rad d^{-1}, respectively. This value of Ω_{eq} translates to an equatorial rotation period for R58 of 0.5641 ± 0.0004 d (given in Table 4). The value of dΩ means that the equator of R58 will take $\sim 250^{+380}_{-90}$ d to lap the poles.

Fig. 15 shows that the peak of the fractional spottedness of R58 shifts to slightly lower latitudes for higher inclination angles. This shift in the latitude distribution of the spots with inclination angle may also impact upon the measured surface differential rotation of R58. Thus, we have calculated the surface differential rotation of R58 for inclination angles of 50° and 70°, using spot filling factors of 0.07 and 0.12, respectively. An inclination of 50° gave values for Ω_{eq} and dΩ of 11.134 ± 0.009 and 0.016 ± 0.015 rad d^{-1}, respectively, whereas an inclination of 70° gave values of Ω_{eq} and dΩ of 11.140 ± 0.012 and 0.042 ± 0.022 rad d^{-1}, respectively. These results are within errors bars of those for an inclination angle

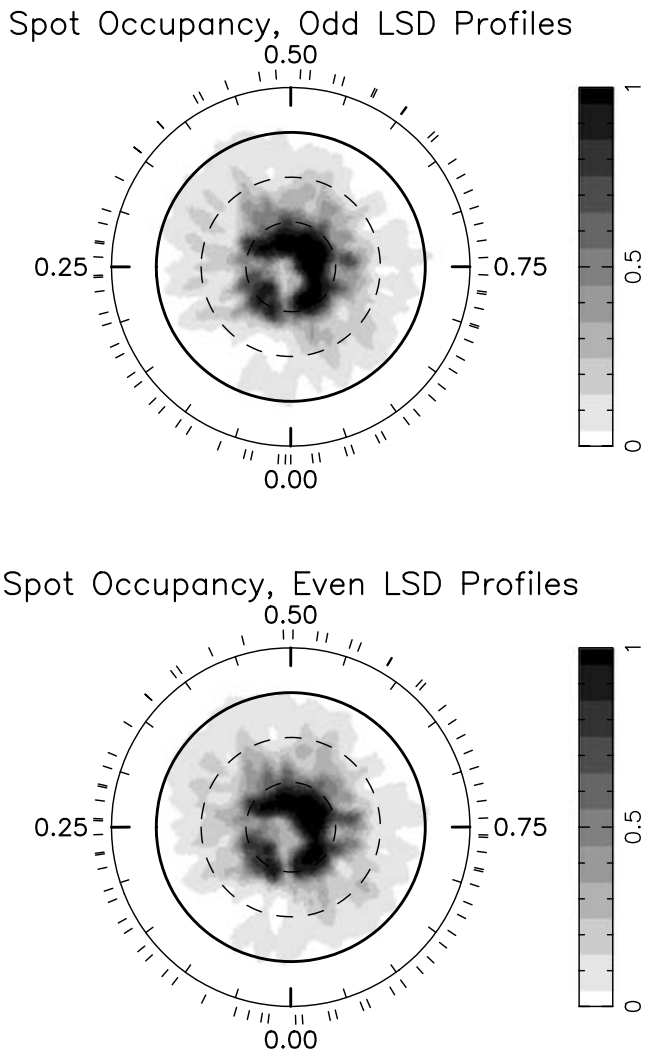

Figure 16. Maximum-entropy brightness image reconstructions for R58, 2000 January 18–21, incorporating photometry using odd-numbered (upper) and even-numbered (lower) LSD profiles. The images are flattened polar projections as described in Fig. 4. The spot filling factor of both images is 0.13.

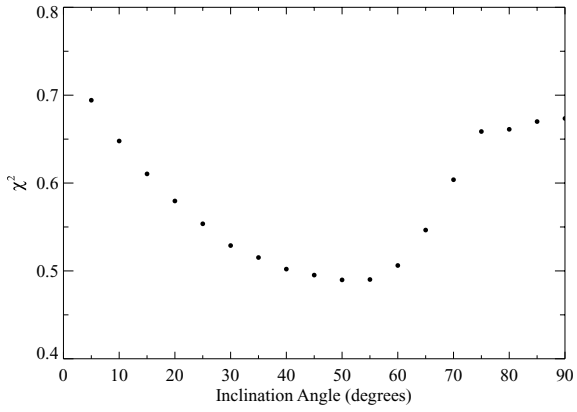

Figure 17. Axial inclination χ^2 minimization for R58. The graph shows the reduced χ^2 values obtained after 25 iterations of the maximum-entropy Doppler imaging code.

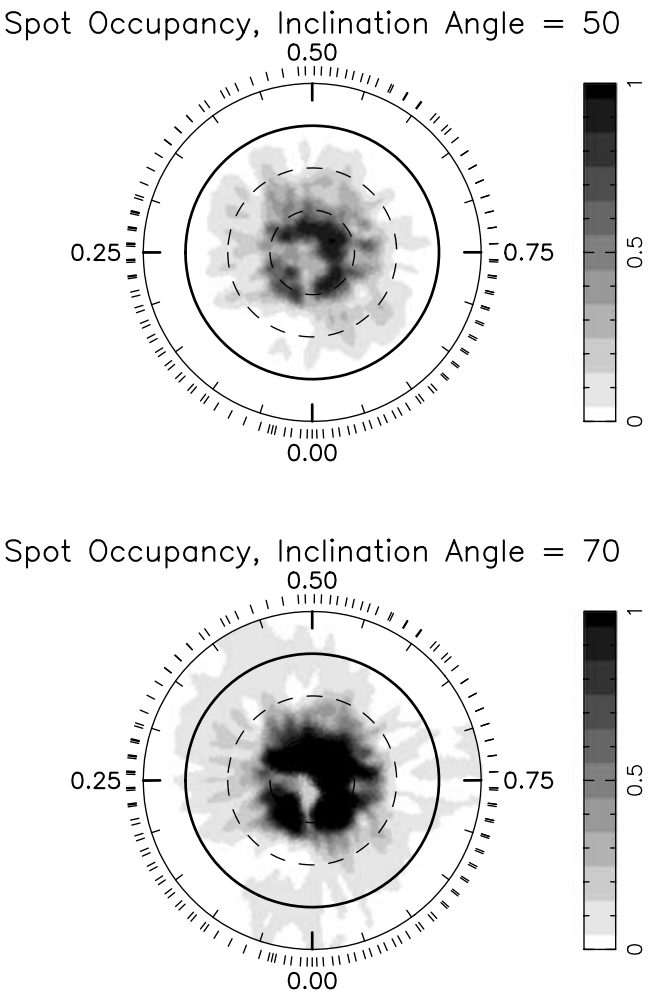

Figure 18. Maximum-entropy brightness image reconstructions for R58, 2000 January 18–21, for an axial inclination angle of 50° (upper) and 70° (lower). The images are flattened polar projections as described in Fig. 4, and the spot filling factor of the two images is 0.10 and 0.17, respectively.

of 60°; however, it would appear that there is some increase in the measured surface differential shear (dΩ) with an increase in the modelled stellar inclination angle.

5 DISCUSSION

The maximum-entropy reconstructed image for R58 (contamination removed) in Fig. 7, shows that R58 possesses a large polar spot extending down beyond ∼60° latitude, along with numerous lower-latitude features. However, this polar spot would appear to be broken with gaps at phases of ∼0.00 and ∼0.25. A comparison of the reconstructed images in Figs 4 and 7 show that the removal of the central contamination in the LSD profiles has little effect on the reconstruction of the low- and mid-latitude features, while reconstructing the polar features of the star. Because the contamination in the LSD profiles matches the radial velocity of the star, the information from the polar regions of R58 always coincides with the contaminated region, making it difficult to recover the information on the spot occupancy of the polar region of R58. The reconstructed polar features in Fig. 7 may actually be stronger or weaker if the amount of contamination has been under- or over-estimated.

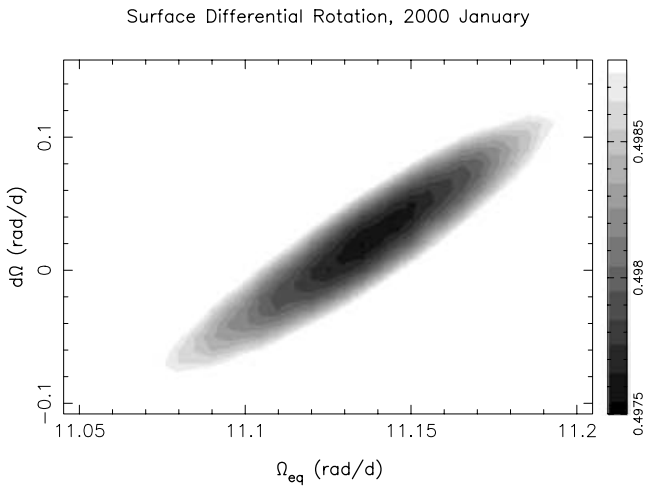

Figure 19. Surface differential rotation χ^2 minimization for R58. The image shows the reduced χ^2 values obtained from the maximum-entropy Doppler imaging code for a fixed spot coverage of 0.09 and an inclination angle of 60°, with darker regions corresponding to lower reduced χ^2 values. The grey-scale image projects $\pm 6\sigma$ on to the axes in both $\Omega_{\rm eq}$ and $\mathrm{d}\Omega$.

Polar spot features are a common occurrence of the surface images of rapidly rotating stars, although the ultrarapid rotator Speedy Mic (Barnes et al. 2001a) appeared to show no evidence of a polar spot. Polar spots, however, are not predicted in theoretical models of the flux emergence on rapidly rotating stars (e.g. Schüssler et al. 1996). Models for rapidly rotating solar-type stars by Granzer (2004) and Granzer et al. (2000) have also shown that solar-type ZAMS stars should produce spots at high, but not polar, latitudes. They have suggested that some other mechanism, such as meridional flow, must be responsible for the transport of spot features to polar latitudes. Schrijver & Title (2001) showed that by simulating a star with 10 times the activity of the Sun, but with other solar parameters, a polar cap was able to be created by meridional flow.

While the brightness reconstructions of R58 show a strong polar feature, the images also show that R58 possesses lower-latitude features, extending from the polar spot down to below 30° latitude. The incorporation of photometry into the image reconstruction process led to, as may be expected, a marked increase in the spot occupancy at low- and mid-latitudes. Low-latitude features are also seen (to varying extents) on almost all early-G dwarfs imaged so far (Strassmeier & Rice 1998; Donati et al. 2000; Barnes et al. 2001b; Rice & Strassmeier 2001; Jeffers et al. 2002; Strassmeier et al. 2003). A table listing the spot distributions on G dwarfs with Doppler images is given by Strassmeier et al. (2003, table. 4). The thin flux tube models of Granzer (2004) predict that for a 1.2-$\mathrm{M}_{\odot}$, ZAMS star (similar to R58) with a rotation rate 63 times the solar value (slightly higher than R58, $\Omega_{\rm R58} \sim 47\ \Omega_{\odot}$) spot locations on such a star can vary from ∼15° up to ∼60° latitude. This agrees quite well with the range of low- to mid-latitude features seen on R58 (Fig. 7).

One of the major processes driving the solar dynamo is differential rotation within the Sun. In the Sun the observed surface differential rotation is known to extend to the base of the convective zone and is responsible for the conversion of a weak poloidal field into a strong toroidal field (the Ω-effect). Thus, measuring differential rotation on the surface of other solar-type stars can be an indicator of the dynamo process occurring within these stars. Fig. 19 indicates that the surface of R58 is rotating almost as a solid body, with a small differential rotation following a solar-like law in that the equator is more rapidly rotating than the poles. Other stars that have had their surface differential rotation measured using the same technique as here have also shown this solar-like differential rotation (see Barnes et al. 2005). However, antisolar differential rotation, in which the equator rotates slower than the poles, has been reported by others for the RS CVn star HR 1099 (e.g. Vogt et al. 1999; Strassmeier & Bartus 2000). Nevertheless, these authors have used a different method (star-spot tracking) for determining differential rotation and Strassmeier & Bartus claim that meridional flow and crosstalk between features may be complicating the issue.

R58 is only the second early-G dwarf with surface differential rotation measured using the method described here. The other is the G2 star LQ Lup (Donati et al. 2000). LQ Lup is very similar to R58, with an age of 25 ± 10 Myr, a mass of $1.16 \pm 0.04\ \mathrm{M}_{\odot}$, and a radius of $1.22 \pm 0.12\ \mathrm{R}_{\odot}$. The differential rotation ($\mathrm{d}\Omega$) measured for LQ Lup is much higher than that measured for R58 here, with $\mathrm{d}\Omega = 0.12 \pm 0.02$ rad d^{-1}. LQ Lup has a rotational period (0.31 d, $\Omega_{\rm eq} = 20.28 \pm 0.01$ rad d^{-1}) nearly half that of R58. The equatorial regions of LQ Lup lap the poles every 50 ± 10 d, implying a photospheric shear two to three times that of the Sun and approximately five times that of R58 in 2000 January.

Are these differential rotation measurements typical for G dwarfs? R58 has been re-observed over a longer time base (∼6 d, compared with the ∼3 d time base here) during 2003 March (preliminary results presented in Marsden et al. 2004). It was found that the differential rotation of R58 during these observations was significantly higher than that measured here, with $\Omega_{\rm eq} = 11.20 \pm 0.01$ and $\mathrm{d}\Omega = 0.14 \pm 0.01$ rad d^{-1}. The K-dwarf star LQ Hya has also shown large variations in its measured differential rotation, from a differential rotation around four times solar ($\mathrm{d}\Omega = 0.1942 \pm 0.0216$ rad d^{-1}) to nearly solid-body rotation ($\mathrm{d}\Omega = 0.0144 \pm 0.0029$ rad d^{-1}) in a year (Donati, Collier Cameron & Petit 2003). Temporal variation in surface differential rotation has also been observed for the K-dwarf AB Dor, although the changes are significantly less than those of LQ Hya, with $\Delta\mathrm{d}\Omega \sim 0.02$ rad d^{-1} (Donati et al. 2003). We believe such changes are evidence of the time-variable dynamo magnetic field having a feedback effect on the dynamics of the convective zone of the star.

The relationship between the level of photospheric shear and stellar parameters, such as rotation rate and convective zone depth, is starting to become clearer as more measurements of differential rotation become available. Using the Doppler imaging method Barnes et al. (2005) have shown that there appears to be an increase in the magnitude of differential rotation with increasing stellar temperature (and thus inversely with convective zone depth) for rapidly rotating spotted (active) stars. These results also showed that there was no significant dependence of differential rotation on stellar rotation rate. Some questions, however, still remain. As mentioned above some stars show temporal variations in their differential rotation, also the Barnes et al. (2005) result of increased differential rotation with increased mass appears contrary to the findings of Reiners & Schmitt (2003). Using line profile analysis Reiners & Schmitt (2003) find that for rapidly rotating non-spotted F-stars the amount of relative differential rotation ($\mathrm{d}\Omega/\Omega_{\rm eq}$) was reduced for $v \sin i \gtrsim 50$ km s^{-1}. Although, this result may be influenced by a decrease in sensitivity with an increase in $\Omega_{\rm eq}$ for faster rotators.

As the Doppler imaging method for determining surface differential rotation has been primarily used to measure differential rotation on lower-mass solar-type stars (i.e. K and early M dwarfs), further observations of the differential rotation of solar-type stars (especially the more massive late-F and early-G dwarfs), at

differing epochs, are required to further define the relationship between differential rotation and stellar parameters.

6 CONCLUSIONS

In this paper, Doppler imaging of the young solar-type star R58 shows that rapidly rotating stars have vastly different photospheric spot features compared with those of the modern-day Sun. The Doppler images produced here show a vast polar cap extending down past 60° latitude and numerous lower-latitude features extending down to the equator of R58. This image is consistent with that demonstrated on Doppler images of other young rapidly rotating G dwarfs.

The differential rotation measurements of R58 would appear to show that in 2000 January it was rotating as more of a solid body than the Sun with a photospheric shear approximately half that of the solar value. The sign of the differential rotation would appear to match that of the Sun with the equator rotating faster than the poles. The amount of photospheric shear was approximately 20 per cent of that seen on the similar, but more rapidly rotating, G2 dwarf LQ Lup.

It is hoped that a long-term data set, similar to that produced for the K dwarfs LQ Hya and AB Dor (Donati et al. 2003) can be produced for (more massive) G dwarfs such as R58.

ACKNOWLEDGMENTS

The observations in this paper were obtained with the AAT and the RSAA 1-m telescope. We would like to thank the technical staff of both the RSAA and the AAO for their excellent assistance during the observations. SCM was funded by a USQ PhD scholarship during the course of this work.

REFERENCES

Barnes J. R., Collier Cameron A., Unruh Y. C., Donati J.-F., Hussain G. A. J., 1998, MNRAS, 299, 904
Barnes S. A., Sofia S., Prosser C. F., Stauffer J. R., 1999, ApJ, 516, 263
Barnes J. R., Collier Cameron A., James D. J., Donati J.-F., 2000, MNRAS, 314, 162
Barnes J. R., Collier Cameron A., James D. J., Donati J.-F., 2001a, MNRAS, 324, 231
Barnes J. R., Collier Cameron A., James D. J., Steeghs D., 2001b, MNRAS, 326, 1057
Barnes J. R., Lister T. A., Hilditch R. W., Collier Cameron A., 2004a, MNRAS, 348, 1321
Barnes J. R., James D. J., Collier Cameron A., 2004b, MNRAS, 352, 589
Barnes J. R., Collier Cameron A., Donati J.-F., James D. J., Marsden S. C., Petit. P., 2005, MNRAS, 357, L1
Bessell M. S., Castelli F., Plez B., 1998, A&A, 333, 231
Brown S. F., Donati J.-F., Rees D. E., Semel M., 1991, A&A, 250, 463
Collier Cameron A., 1992, in Byrne P. B., Mullan D. J., eds, Surface Inhomogeneities on Late-Type Stars. Springer-Verlag, Berlin, p. 33
Donati J.-F., Brown S. F., 1997, A&A, 326, 1135
Donati J.-F., Semel M., Carter B., Rees D. E., Cameron A. C., 1997, MNRAS, 291, 658
Donati J.-F., Mengel M., Carter B. D., Marsden S., Collier Cameron A., Wichmann R., 2000, MNRAS, 316, 699
Donati J.-F., Collier Cameron A., Petit P., 2003, MNRAS, 345, 1187
Graham J. A., 1982, PASP, 94, 244
Granzer T., 2004, Astron. Nachr., 325, 417
Granzer T., Schüssler M., Caligari P., Strassmeier K. G., 2000, A&A, 355, 1087
Jeffers S. V., Barnes J. R., Collier Cameron A., 2002, MNRAS, 331, 666
Kurucz R. L., 1993, CDROM #13 (ATLAS9 atmospheric models) and CDROM no 18 (ATLAS9 and SYNTHE routines, spectral line database)
Marsden S. C., Waite I. A., Carter B. D., Donati J.-F., 2004, Astron. Nachr., 325, 246
Petit P., Donati J.-F., Collier Cameron A., 2002, MNRAS, 334, 374
Petit P. et al., 2004, MNRAS, 351, 826
Prosser C. F., Randich S., Stauffer J. R., 1996, AJ, 112, 649
Randich S., Schmitt J. H. M. M., Prosser C. F., Stauffer J. R., 1995, A&A, 300, 134
Reiners A., Schmitt J. H. M. M., 2003, A&A, 412, 813
Rice J. B., Strassmeier K. G., 2001, A&A, 377, 264
Schrijver C. J., Title A. M., 2001, ApJ, 551, 1099
Schüssler M., Caligari P., Ferriz-Mas A., Solanki S. K., Stix M., 1996, A&A, 314, 503
Siess L., Dufour E., Forestini M., 2000, A&A, 358, 593
Skilling J., Bryan R. K., 1984, MNRAS, 211, 111
Stauffer J. R., Hartmann L. W., Prosser C. F., Randich S., Balachandran S., Patten B. M., Simon T., Giampapa M., 1997, ApJ, 479, 776
Strassmeier K. G., Bartus J., 2000, A&A, 354, 537
Strassmeier K. G., Rice J. B., 1998, A&A, 330, 685
Strassmeier K. G., Pichler T., Weber M., Granzer T., 2003, A&A, 411, 595
Sung H., Bessell M. S., 2000, PASA, 17, 244
Unruh Y. C., Collier Cameron A., 1995, MNRAS, 273, 1
van Leeuwen F., 1999, A&A, 341, L71
Vogt S. S., Hatzes A. P., Misch A. A., Kürster M., 1999, ApJS, 121, 547
Wade G. A., Donati J.-F., Landstreet J. D., Shorlin S. L. S., 2000, MNRAS, 313, 823
Whiteoak J. B., 1961, MNRAS, 123, 245

This paper has been typeset from a TEX/LATEX file prepared by the author.